iScience

CellPress
OPEN ACCESS

Article

The developmental profile of visual cortex astrocytes

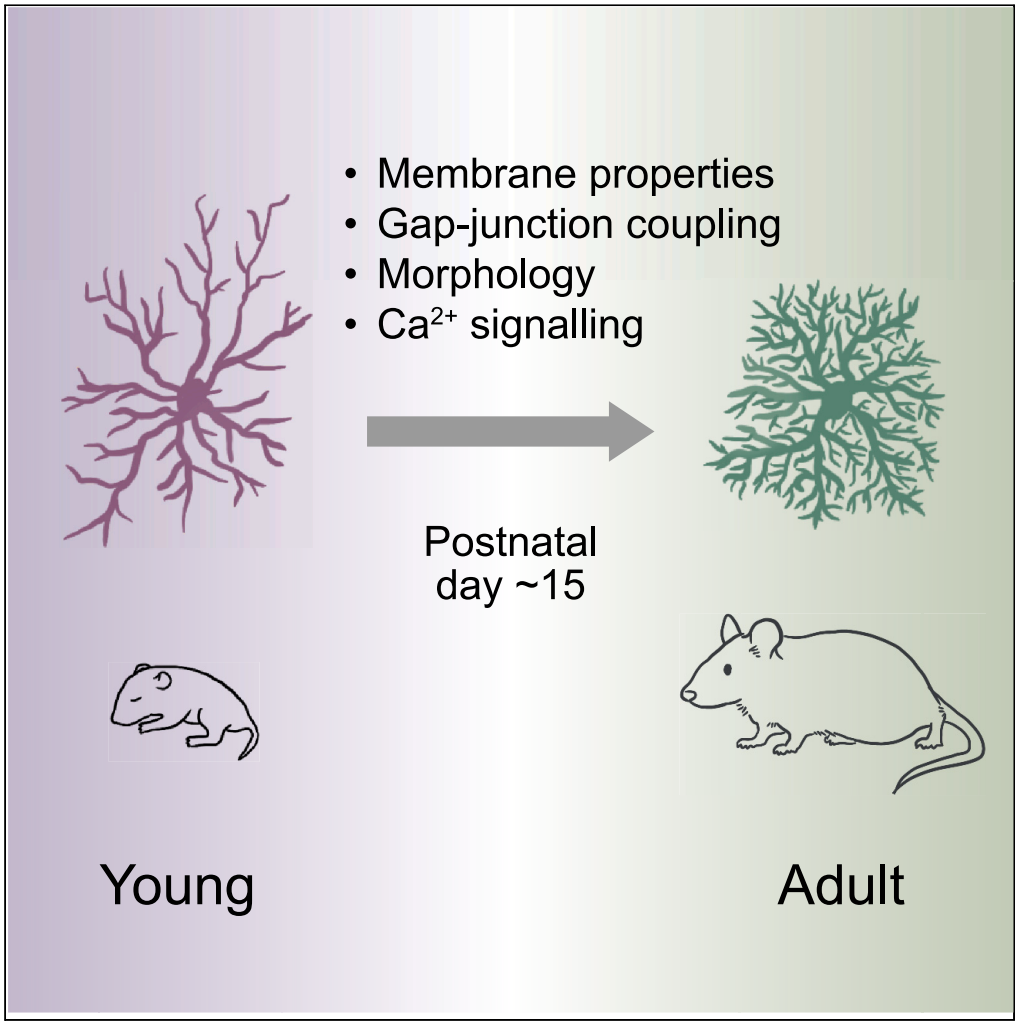

Airi Watanabe, Connie Guo, Per Jesper Sjöström

jesper.sjostrom@mcgill.ca

Highlights

Astrocyte biophysics, gap-junction coupling, and morphology developed in parallel

Spontaneous Ca^{2+} activity decorrelated, increased in rate, and decreased in duration

Most properties stabilized by ~P15, although morphology continued to develop

Watanabe et al., iScience *26*, 106828
June 16, 2023
https://doi.org/10.1016/j.isci.2023.106828

iScience

CellPress
OPEN ACCESS

Article

The developmental profile of visual cortex astrocytes

Airi Watanabe,[1,2] Connie Guo,[1,3] and Per Jesper Sjöström[1,4,*]

SUMMARY

We investigated how astrocytes in layer 5 mouse visual cortex mature over postnatal days (P) 3–50. Across this age range, resting membrane potential increased, input resistance decreased, and membrane responses became more passive with age. Two-photon (2p) and confocal imaging of dye-loaded cells revealed that gap-junction coupling increased starting ~P7. Morphological reconstructions revealed increased branch density but shorter branches after P20, suggesting that astrocyte branches may get pruned as tiling is established. Finally, we visualized spontaneous Ca^{2+} transients with 2p microscopy and found that Ca^{2+} events decorrelated, became more frequent and briefer with age. As astrocytes mature, spontaneous Ca^{2+} activity thus changes from relatively cell-wide, synchronous waves to local transients. Several astrocyte properties were stably mature from ~P15, coinciding with eye opening, although morphology continued to develop. Our findings provide a descriptive foundation of astrocyte maturation, useful for the study of astrocytic impact on visual cortex critical period plasticity.

INTRODUCTION

Historically, astrocytes have been chiefly considered as structural support cells in the central nervous system. For example, they hold neuronal components together, maintain molecular homeostasis, and control the blood–brain barrier.[1] One reason that astrocytes were mainly thought of as passive players is that their excitability is poor compared to neurons, e.g., astrocytes cannot propagate action potentials. However, in the early 1990s, it was discovered that these glia cells do in fact exhibit active responses, although via Ca^{2+} signals.[2,3] Soon after this discovery, it was established that following cytosolic Ca^{2+} elevation astrocytes respond to neurotransmitters by releasing gliotransmitters.[4,5] Moreover, stimulation of a single astrocyte can trigger a wave of intracellular Ca^{2+} that propagates from astrocyte to neighboring astrocyte via gap junctions — channels specialized for cell-to-cell communication.[4,6]

Astrocytes have since been implicated in several central nervous system functions, including synaptic plasticity,[7,8] regulation of neuronal excitability[9] and memory formation.[10,11] Importantly, a single mature astrocyte contacts over 100,000 synapses with each astrocyte occupying tiles, i.e., exclusive, non-overlapping territories.[12] Therefore, they are in strategic positions to modulate synapses within tiles. On the other hand, gap junctions allow Ca^{2+} signals to propagate in the interconnected astrocyte syncytium network. Gap-junction coupling thus expands the modulation range of astrocytes beyond the tile.[13]

Ca^{2+} signaling in astrocytes occurs either spontaneously or in response to neurotransmitter stimulation.[14,15] These Ca^{2+} signals — which are relevant for basal synaptic function[16] — originate in microdomains of astrocyte processes and propagate to other regions of the cell[17,18] as well as to neighboring astrocytes.[19] This astrocyte Ca^{2+} activity triggers the release of gliotransmitters, such as D-serine, ATP, and glutamate.[20] For example, astrocyte Ca^{2+} signaling actively participates in the induction of neocortical spike-timing-dependent plasticity.[21] A key remaining question, however, is how the morphological development of astrocytes is coordinated with the maturation of intracellular Ca^{2+} signaling, which has implications for astrocytic control of neocortical plasticity.[21]

In mouse visual cortex, the critical period starts around P20 and ends around P35,[22] although weaker and qualitatively different plasticity persists beyond P35.[23] Circuits refine rapidly as sensory input increases with eye opening, typically around ~P13.[24] During this postnatal period, neuronal morphologies mature by

[1]Centre for Research in Neuroscience, Brain Repair and Integrative Neuroscience Program, Department of Medicine, The Research Institute of the McGill University Health Centre, Montreal General Hospital, Montreal, QC H3G 1A4, Canada

[2]Integrated Program in Neuroscience, Irving Ludmer Building, McGill University, 1033 Pine Avenue West, Montreal, QC H3A 1A1, Canada

[3]Department of Anatomy and Cell Biology, Faculty of Science, McGill University, Strathcona Anatomy and Dentistry Building, 3640 University Street, Montreal, QC H3A 0C7, Canada

[4]Lead contact

*Correspondence: jesper.sjostrom@mcgill.ca

https://doi.org/10.1016/j.isci.2023.106828

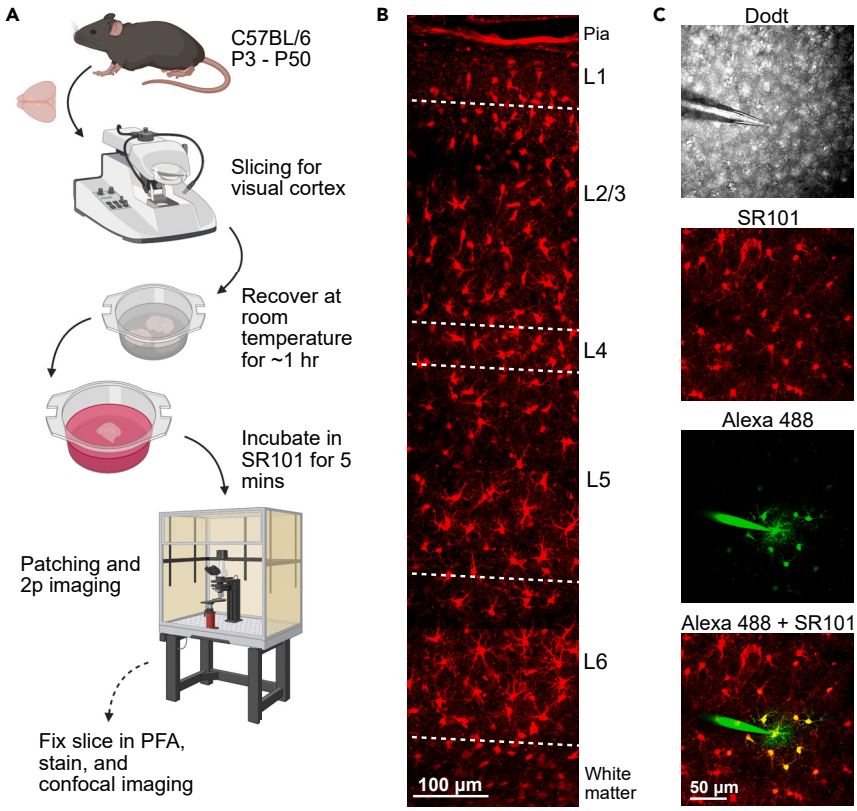

Figure 1. Astrocytes were targeted using SR101

(A) Acute slices were obtained from C57BL/6 mice and subsequently incubated in a container of ACSF to recover at room temperature for 1 h. Before patching, a slice was transferred to a 6-well plate or Petri dish filled with 1 or 5 µM SR101 for 5 min. A homemade mesh holder and bubbler allowed slices to sit on the mesh while the bubbler infused carbogen (not depicted) into the SR101 solution to keep the slice oxygenated. The slice was then transferred to the bath chamber of an electrophysiology rig for patching. After patching, the slice was either discarded or fixed in PFA for further analyses (optional dashed arrow). Schematic created in BioRender is for illustration purposes and does not show exact equipment used (see STAR Methods).

(B) Sample cortical stack of acute slice after pre-incubation in 1 µM SR101; Astrocytes in all cortical layers could be visualized under 2p microscopy at 930 nm.

(C) SR101-labelled astrocytes (red) were targeted and patched with pipette filled with Alexa Fluor 488 (80 µM, green). The Alexa dye spread to neighboring astrocyte soma (yellow), presumably through gap junctions.

adding branch complexity and synaptic spines,[25] and some studies in other brain areas indicate that development of astrocyte complexity mirrors this progression.[26,27] However, visual cortex astrocytes development has not been as well studied.

We therefore explored how electrophysiological and morphological properties of layer 5 (L5) visual cortex astrocytes mature with age. We found that, over development, astrocytes elaborated denser arborizations, spontaneous Ca^{2+} activity in individual astrocytes decorrelated, and Ca^{2+} events increased in frequency as well as decreased in duration. Astrocyte morphology matured by becoming denser, more compact, and more symmetric. Several astrocyte properties stabilized around P15, including gap-junction coupling, morphology, membrane biophysics, and Ca^{2+} signaling.

RESULTS

Diverse astrocyte electrophysiology matured with age

To explore astrocyte electrophysiology within L5 visual cortex, we targeted astrocytes in P3 – P50 acute mouse brain slices for whole-cell patching. We pre-incubated acute slices in 1 or 5 µM SR101 (see STAR Methods), a fluorescent dye that is selectively taken up by astrocytes (Figure 1A).[28,29] With 2p imaging

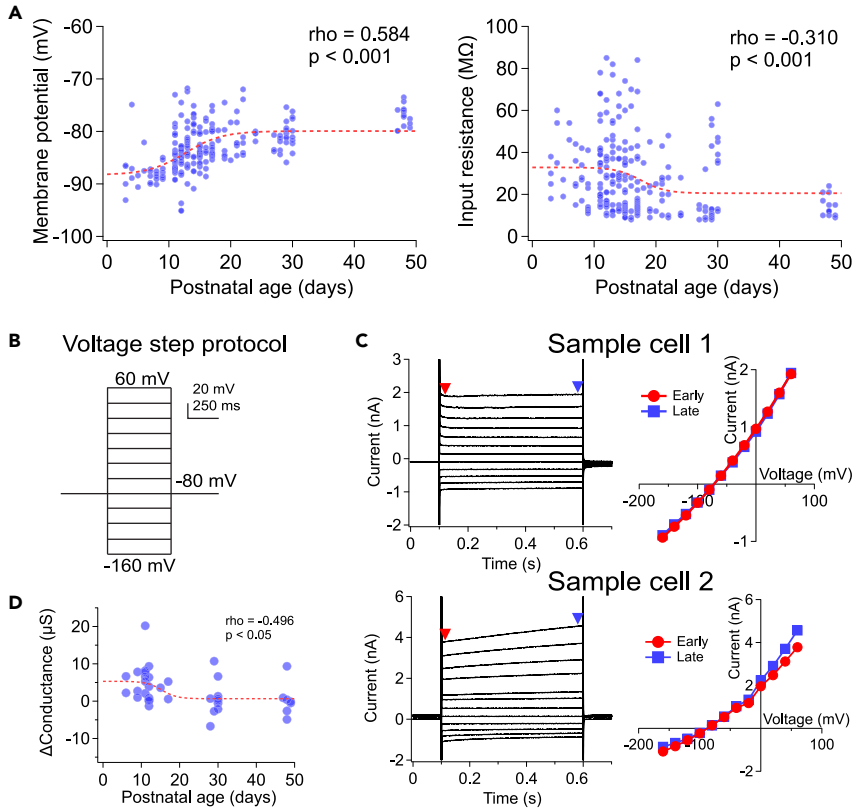

Figure 2. Membrane conductance properties were heterogeneous and matured with age

(A) Over development, resting V_m depolarized and R_{input} decreased.

(B) To assess membrane biophysics, voltage steps of 20 mV decrements from +60 mV to −160 mV were applied to patched astrocytes.

(C) Sample IV curves from two cells show different membrane conductance properties. Red arrowhead and round data points indicate early current readings (10 ms after start of voltage step) and, blue arrowhead and square data points indicate late current readings (10 ms before the end of voltage step).

(D) The late-early conductance difference (see STAR Methods) decreased as astrocytes matured (n = 39 cells, N = 17 animals).

at 820 nm, we were able to visualize astrocyte staining in all cortical layers (Figure 1B), which enabled us to identify astrocytes for targeted patching (Figure 1C).

Astrocyte identity was confirmed by verifying that the cell had characteristic passive properties,[30,31] including hyperpolarized resting membrane potential (V_m, −83 ± 0.3 mV, n = 222 cells, N = 78 animals) and low input resistance (R_{input}, 28 ± 1.2 MΩ). However, we found that R_{input} and V_m were variable, suggesting heterogeneity among astrocytes (Figure 2A). Despite this heterogeneity, we could observe that astrocyte V_m increased with age, and that R_{input} decreased (Figure 2A).

To further investigate the membrane properties of astrocytes over development, we applied voltage steps from +60 mV to −160 mV to the patched cells (Figure 2B). We saw cells exhibiting heterogeneous membrane conductance properties, with some displaying passive current readings in response to the voltage steps (Figure 2C, top), and others showing a time-dependent current, especially in the more depolarizing voltage steps (Figure 2C, bottom). To see if the time-dependent component varied with age, we quantified this as the difference in conductance between the late and early stages of the voltage step (ΔConductance; see STAR Methods) and compared this over development, which revealed that it decreased with age (Figure 2D).

Gap-junction formation might affect electrophysiological properties

We explored whether the changes observed in electrophysiological properties correlated with the development of gap -junctions in astrocytes. It is well known that astrocytes couple with neighboring astrocytes

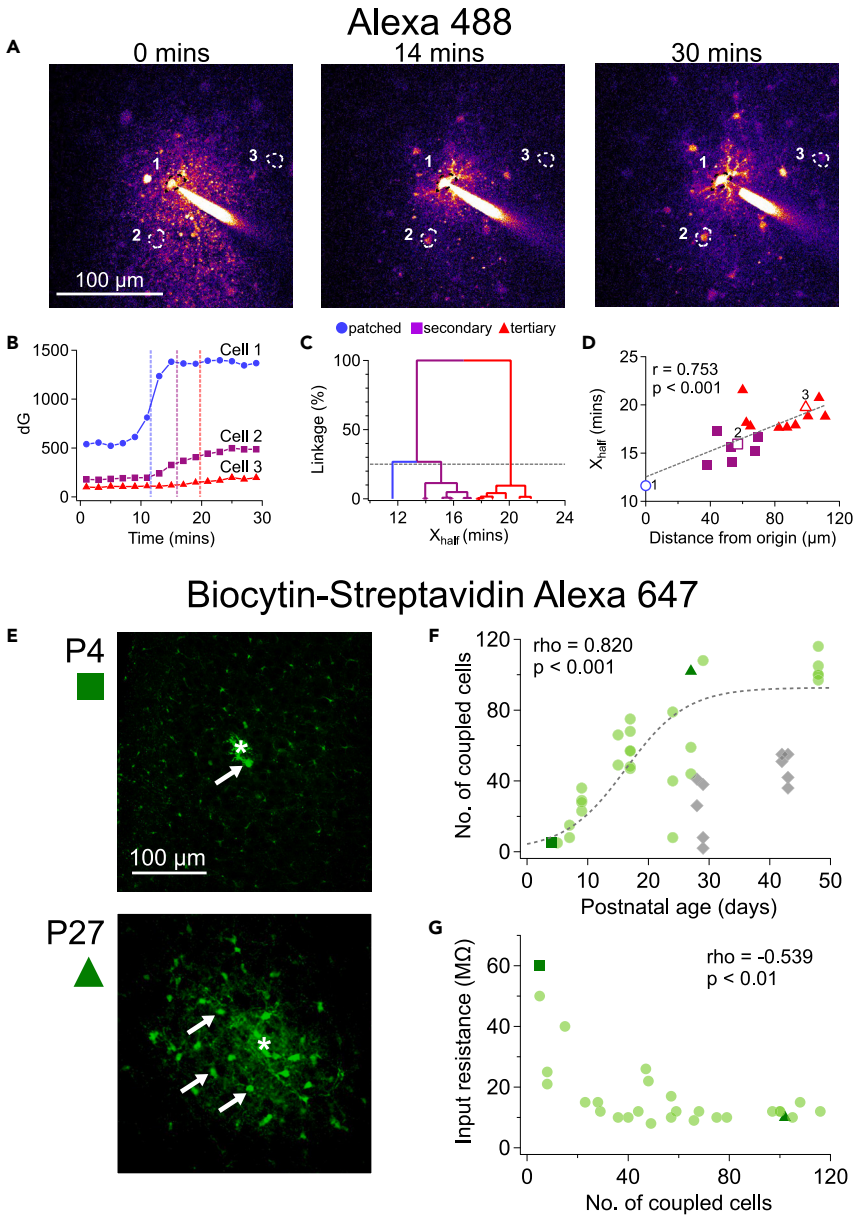

Figure 3. Astrocyte gap-junction coupling increased with age

(A) Sample 2p image shows Alexa 488 dye from patched astrocyte 1 spreading to example neighboring astrocytes 2 and 3 (dashed outlines) over time.

(B) The fluorescence intensity signal of three sample astrocytes (1, 2, 3) in panel A increased. Fluorescence time courses and maxima were consistent with Cell 2 (purple) dye-filling directly from Cell 1 (blue), but Cell 3 (red) indirectly dye-filling from a secondary astrocyte such as Cell 2. Dashed lines denote the x_{half} half-max time points of sigmoidal fits (not shown).

(C) The 25% best cut (dashed line) of hierarchically clustered x_{half} values independently suggested three fluorescence-onset clusters, consistent with the patched cell (blue) first dye-filling secondary astrocytes (purple), and those indirectly dye-filling tertiary cells (red) in a gap-junction-coupled astrocyte network.

(D) Consistent with progressive dye-filling of a gap-junction-coupled astrocyte network, the fluorescence half-max x_{half} (see B, C) correlated positively with distance from patched astrocyte. Secondary (purple) and tertiary astrocyte labels (red) are based on clustering in C. Blue open circle is Cell 1 in A, purple open square is Cell 2, and red open triangle is Cell 3.

(E) Because gap junctions may restrict passage of relatively large Alexa488 dye molecules, we redid the experiments in A-D by dialyzing patched cells (asterisks) with biocytin, which is permeable through all astrocytic connexin channels (Stephan et al., 2021). After histochemistry and confocal imaging (see STAR Methods), neighboring stained cells were

Figure 3. *Continued*
counted (examples indicated by arrows). With this approach, sample P4 astrocytes did not dye-couple as much as sample P27 astrocytes did.
(F) The biocytin approach indicated that gap-junction coupling increased over development (green symbols, n = 28 patched cells, N = 12 animals) and then apparently plateaued > P20. Square indicates P4 sample cell and triangle indicates P27 sample cell depicted in (E). After carbenoxolone treatment, fewer cells were labeled for ages > P20 (gray diamonds, not included in sigmoid fit, n = 10 patched cells, N = 4 animals, $p < 0.01$, Wilcoxon-Mann-Whitney), suggesting that developmental gap junction formation caused the increase in dye coupling with age.
(G) R_{input} decreased with the number of coupled cells, consistent with gap junctions making astrocytes electrically leakier.

through connexin gap junctions.[30,32] Therefore, we first patched individual astrocytes and dye-filled them with Alexa Fluor 488 for 30 min while taking time-lapse images every 2 min to visualize dye spreading to neighboring cells (Figure 3A and Video S1). The rate of dye filling in astrocytes was quantified by measuring fluorescence intensity in a soma-centered ROI over time (Figure 3B). The fluorescence intensity curves were fitted with sigmoids to obtain their x_{half} values, i.e., the time at which cells were half filled. When these x_{half} values were independently clustered using a hierarchical agglomerative approach, two distinct groups emerged (purple, red, Figure 3C). A positive correlation was also found between the x_{half} time and the distance between the neighbor and patched astrocyte (Figure 3D). The two clustered groups likely correspond to primary neighbors that are coupled directly to the patched astrocyte (Figures 3C and 3D, purple and square) and secondary neighbors that are coupled to primary neighbors (Figures 3C and 3D, red and triangle). Finally, the x_{half} for secondary astrocytes (19 $\pm$ 0.4 min, n = 10) was larger than that of primary astrocytes (16 $\pm$ 0.5 min, n = 7; $p < 0.001$). These data indicate that primary neighbors closer to the patched astrocyte get dye-filled first, followed by secondary neighbors, on the timescale of minutes. Because Alexa 488 does not readily pass through connexin-30-containing gap junctions,[33] we opted to repeat the cell counts using biocytin, which is small enough to permeate astrocytic connexin channels.[33] After biocytin histochemistry (see STAR Methods), we counted the number of dye-filled neighboring astrocytes (Figure 3E) and found that this number increased with age (Figure 3F, green markers). To verify that dye coupling relied on gap junctions, we did a subset of experiments at P28 – P43 using carbenoxolone, a non-selective connexin and pannexin hemichannel blocker[34] (Figure 3F, gray markers). We found that carbenoxolone reduced the number of coupled cells by approximately 40% (Figure 3F), consistent with reports that carbenoxolone do not completely block gap junctions.[35] We also found that gap-junction coupling correlated with a decrease in R_{input} (Figure 3G). Taken together, our data suggested that over development, astrocytes formed more gap junctions with their neighbors and/or that gap junctions became more permeable (Figure 3G).

Astrocyte arbors became denser, more compact, and more symmetric with age

To explore astrocyte morphology development, we manually reconstructed astrocytes at different ages from images obtained either with 2p or confocal imaging (Figure 4A). We categorized cells obtained from animals into 4 age groups, those aged P1 – P10 (yellow), P11 – P20 (cyan), P21 – P30 (magenta), and P41 – P50 (green) for further comparison. To look at the extent of branching in these four groups, we compared the convex hulls which measure the maximal reach of a cell's processes. Surprisingly, although we expected the convex hulls to expand with age (i.e., that astrocytes became larger with age), they were mostly indistinguishable (Figure 4B). However, when we looked at the branch density, we found that older astrocytes had more branches close to the soma as seen from a more saturated density heatmap (Figure 4C). This finding was supported by soma-centered Sholl analysis,[36] which showed a higher number of branch crossings close to the soma in old astrocytes (Figure 4D; Spearman's rho = 0.35 for Sholl plot peak versus age, $p < 0.05$). When we looked at the arbor center, i.e., the center of the entire reconstruction, and measured its distance from the soma, we found that astrocytes in the P1 – P10 and P11 – P20 groups had arbor centers further away from the soma compared to those in P21 – P30 and P41 – P50, meaning they were more asymmetric when younger (Figure 4E). When Sholl analysis for the four age groups were considered, we observed that overall, the averaged cumulative number of crossings were greater in the older age groups (Figure 4F). However, >40 μm away from the soma, the younger age groups extend more branches (Figure 4F, inset). Similarly, we found that the cumulative crossings <40 μm away from the soma showed a positive correlation with age (Figure 4G), whereas those >40 μm away correlated negatively (Figure 4G, inset). Taken together, these findings indicate that with age, astrocyte arbors become denser, more compact, and more symmetric.

Astrocyte Ca^{2+} activity decorrelated with age

Astrocytes display spontaneous Ca^{2+} activity in their processes.[37,38] We investigated if this Ca^{2+} activity changed with age. We targeted SR101-stained astrocytes P7 – P50 for patching and dialyzed them with

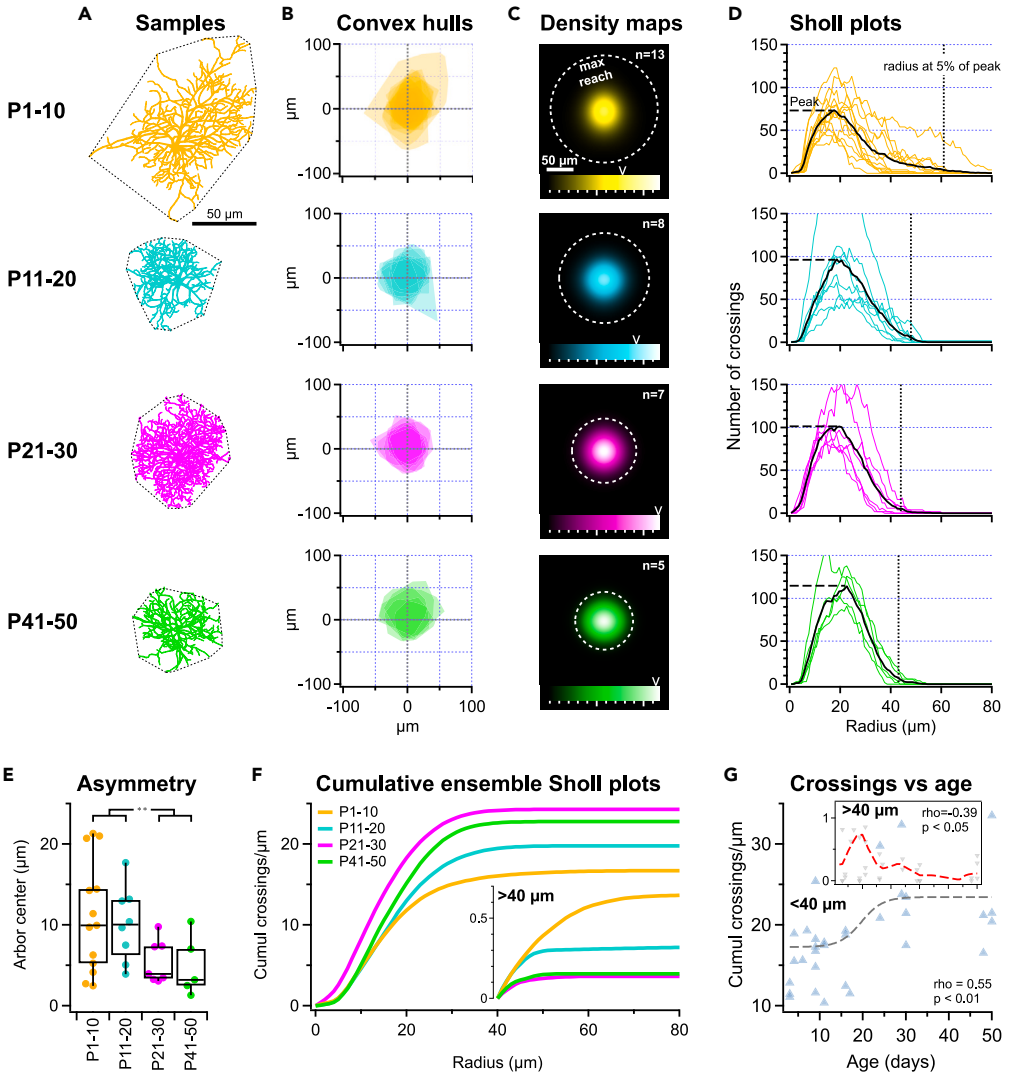

Figure 4. Maturing astrocyte arbors became denser, more compact, and more symmetric

(A) Sample astrocyte reconstructions illustrate how branching became denser, more compact, and more symmetric with age. The convex hull (dotted lines) indicates the maximal reach of branches.

(B) Convex hulls, overlaid and centered on soma, suggested that with age, arbors became more symmetric as well as more compact.

(C) Radially symmetric branch density heat maps (see STAR Methods) suggested increased process branching close to the soma in old astrocytes. However, the farthest-reaching process seemed closer with age (dotted line). To enable comparison across age groups, heatmaps share scale, with map max intensity indicated by arrowhead above color scale.

(D) In agreement with increased branching close to soma over age, Sholl analysis (Sholl, 1953) showed higher peak averages (horizontal dashed lines) whereas 5%-of-peak-average radii (vertical dotted lines) seemed smaller. Colored lines: Sholl plots of individual astrocyte arbors; black lines: age-group averages.

(E) Distance from soma to arbor density center — a measure of arbor asymmetry — indicated that astrocyte arbors became more symmetric with development (ANOVA $p < 0.05$). Boxplots indicate medians and quartiles, with whiskers denoting extremes.

(F) Cumulative ensemble Sholl plots across age groups indicated overall more branching in older astrocytes, although >40 µm from the soma, young astrocytes branched more (inset).

(G) In agreement with arborizations enriching close to the soma, cumulative crossings within a 40 µm radius correlated positively with age (Spearman's rho), plateauing after ~P20. Smoothed 5-day running average (dashed red line) suggested distal branch growth at ~P5 followed by distal branch pruning, hence a negative correlation for >P5 ages for distal branches >40 µm (Spearman's rho).

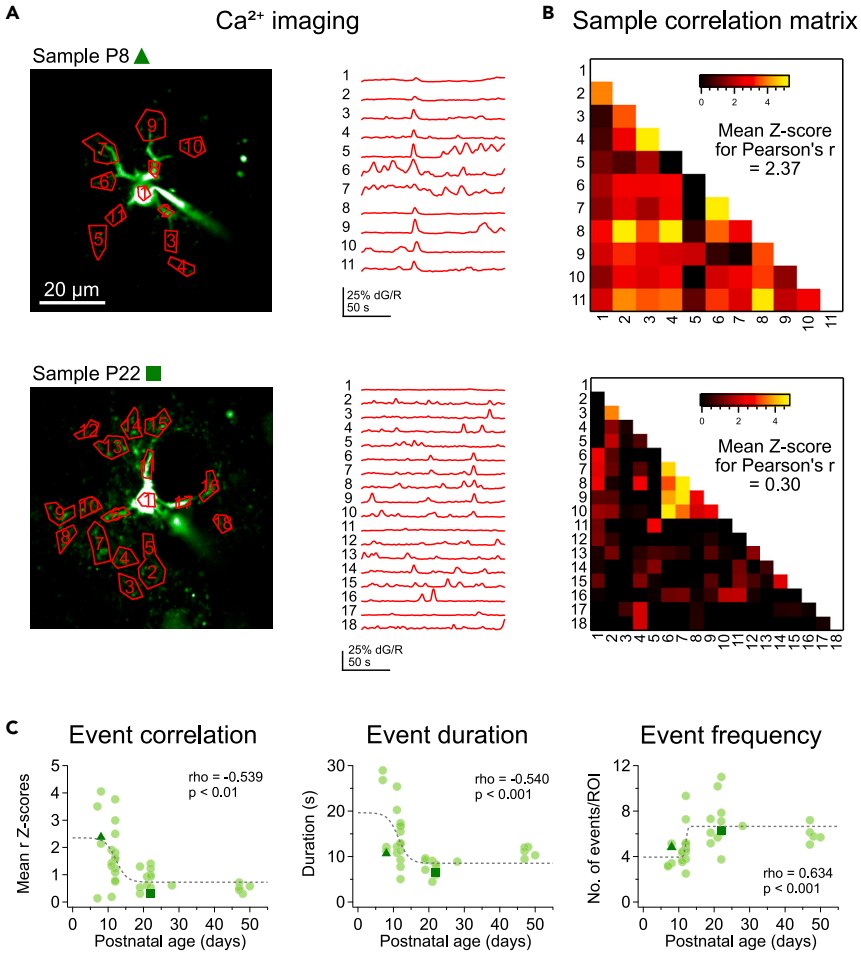

Figure 5. Ca^{2+} events became decorrelated, briefer, and more frequent with age

(A) Fluo-5F Ca^{2+} signals (green) were recorded as a 150-second-long movie (see Videos S1 and S2) of these two sample P8 (triangle) and P22 astrocytes (square). During offline analysis, ROIs (left, red) were manually selected, and fluorescence was quantified as dG/R sweeps (right).

(B) Sample ROI cross-correlation matrices for the astrocytes in A. For each matrix, a single mean *Z*-score Pearson's r was calculated, which was 2.3785 and 0.30477 for the P8 and P22 samples, respectively. Mean *Z*-score served as a metric for how correlated the activity of a cell was.

(C) With age, astrocyte Ca^{2+} events became decorrelated, briefer, and more frequent (n = 36 cells, N = 15 animals), stabilizing approximately beyond P15. Triangle indicates sample P8 cell and square indicates sample P22 cell depicted in (A). See also Figure S1.

the Ca^{2+}-sensitive dye Fluo-5F (200 µM). We acquired 150-second-long videos of a single focal plane and selected ROIs to analyze fluorescent activity (Figure 5A). To assess the similarity in Ca^{2+} activity between different ROIs, we calculated the *Z*-scored Pearson's r pairwise across all ROIs in each recorded astrocyte. This way, we obtained a Ca^{2+} activity correlation matrix for each astrocyte (Figure 5B). This heatmap was averaged to produce a mean *Z*-score for each astrocyte, which represents how correlated the Ca^{2+} activity was in that cell. By plotting astrocyte mean *Z*-score of Pearson's r versus age (Figure 5C), we found that Ca^{2+} activity decorrelated with age. In addition, we also detected and quantified the frequency and duration of individual Ca^{2+} transients and found that spontaneous Ca^{2+} signals became more frequent as well as shorter in duration with age (Figure 5C).

One concern with manual ROI selection is the potential for user bias. To explore this possibility, we first asked if the area of manually selected ROIs varied systematically with age, but it did not (Pearson's r = 0.22, p = 0.20, data not shown). Next, to circumvent manual ROI selection, we used the automated

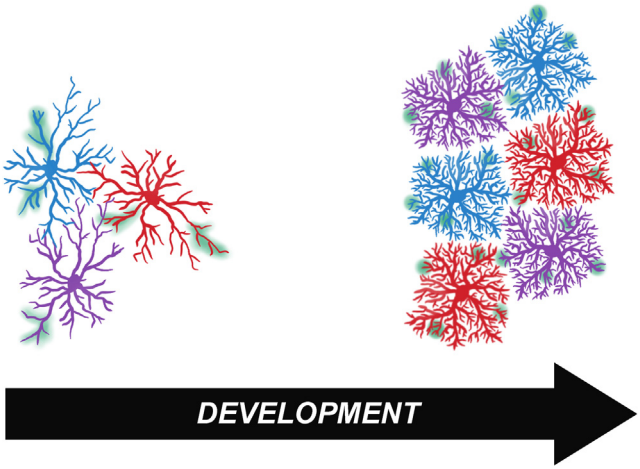

Figure 6. As astrocytes mature, branching, overall numbers, and Ca^{2+} signal compartmentalization increase

Proposed model illustrating key aspects of how young L5 V1 astrocytes — which are asymmetric, relatively far-reaching, and poorly branched (left) — mature by forming denser, more compact, and more symmetric arbors, as well as by growing more plentiful (right) to tile the growing neocortex. Ca^{2+} signals (green) also decorrelated and compartmentalized over development. Most properties stabilized by P15, right around eye opening, although arbors continued to refine by growing denser. See also Figure S2.

Ca^{2+}event detection software AQuA.[39] We found that the spatial density metric of AQuA decreased with age (Figure S1), which means that, as astrocytes matured, events did not co-occur as frequently.

Taken together, these results indicate that early activity was dominated by single, large events that encompassed most or all branches in individual astrocytes (Video S2), whereas in more mature astrocytes, Ca^{2+} transients were more localized, relatively independent of each other, and comparatively brief (Video S3). However, this does not imply that small, localized events never happened in young animals, because early activity was relatively heterogeneous.

Astrocyte density in L5 cortex remains constant while cortical thickness increases

We next measured L5 cortical thickness and found that it rapidly increased around P10, stabilizing at ~250 μm thickness by ~P15 (Figure S2A). Because our morphological reconstructions indicated that astrocytes did not grow larger with development (Figure 4), we wondered if astrocytes increased in numbers to ensure even tiling of the growing cortex. We therefore counted the astrocytes in L5 and saw that their density remained relatively unchanged over age (Figure S2B). Together with our morphological reconstructions (Figure 4), these findings demonstrate that L5 astrocytes grow in number rather than size. In summary, we found that L5 visual cortex astrocytes start off with few, probably partially overlapping branches, little gap-junction coupling, and correlated Ca^{2+} signaling, which mature by growing in numbers as L5 expands, by growing denser branches as tiling is established, by adding functional gap junctions, and by decorrelating Ca^{2+} signals into relatively brief localized events (Figure 6).

DISCUSSION

Here, we studied the development of astrocytes in L5 of visual cortex across the ages P3 – P50. We found that astrocyte electrophysiological properties, although quite heterogeneous, mature by a depolarization of V_m and a reduction of R_{input}. We also found that astrocyte morphology became denser and gap-junction coupling increased with development, and that spontaneous astrocyte Ca^{2+} activity decorrelated (Figure 6). In addition, these Ca^{2+} transients increased in frequency and decreased in duration over the ages studied.

Astrocytes depolarize and become leaky as they mature

Astrocyte biophysics was heterogeneous across cells, with for example R_{input} spanning an order of magnitude, and with some but not all astrocytes carrying a slowly adapting conductance. Despite this variability,

we found developmental changes: With age, astrocytes depolarized and became leakier, whereas the slowly adapting current gradually decreased (Figure 2). At ~P15, membrane properties seemed to stabilize. Overall, our results are consistent with previous findings in L2/3 of the visual cortex.[40]

The heterogeneous electrophysiology we report has previously been found in astrocytes of the striatum, hippocampus, and neocortex.[30,41] It has been argued that such heterogeneity reflects differences in gap-junction coupling[41] or astrocyte types.[30] Anders et al.[42] showed that in the hippocampus gap-junction coupling relates to astrocyte location relative to the pyramidal cell layer, suggesting the existence of layer-dependent astrocyte properties. We, however, only studied astrocytes in L5 of visual cortex, suggesting that the heterogeneity we found is not because of layer location, but more likely gap-junction coupling.[41]

Astrocyte gap-junction coupling first develops in rat visual cortex at P1[32] and then gradually increases.[33] In mouse thalamus, Griemsmann et al.[43] found that astrocyte coupling did not increase after the first two postnatal weeks. In agreement, we found that dye-coupling was stabilized from ~P20 and onwards (Figure 3). This may suggest that developmental gap-junction coupling is linked to the maturation of membrane properties because of a correlation of these properties (Figure 3G), which is also supported by prior experiments done in the striatum.[30]

Astrocyte arbors mature by growing denser and more compact

As expected, astrocytes developed denser arbors as they matured. In alignment with the findings of Bushong et al.[26], our morphometry analysis revealed longer branches in the young compared to the old age group. Young arborizations were also more asymmetric. This suggests that astrocytes first grow long but weakly branched arbors that are subsequently pruned whereas arborizations grow dense close to the soma. In this view, astrocyte branches may dynamically develop by growth and retraction, perhaps to establish even tiling by sampling different territories.

Astrocyte arbors may thus develop like neuronal axons and dendrites do, by initial exuberance followed by subsequent pruning.[44] As tiling boundaries form, the territory covered fills in with additional branches as the astrocyte matures. However, more detailed study is required to verify this growth-and-retraction idea, e.g., by *in vivo* time lapse imaging. Nevertheless, our findings are consistent with e.g., the report of Bushong et al.[26] who found heterogeneous astrocyte morphologies in rat hippocampus before P14. They also found that astrocytes extended long processes and that astrocyte tiling was not consistently seen until P14.[26]

An alternative interpretation is that the astrocyte pruning is only apparent, and that over development, individual astrocyte somata instead migrate toward the center of their arborizations. Because our Sholl analysis was soma-centered (Figures 4D, 4F, and4G), such a soma migration would give rise to an artificial appearance of arbor pruning. Our analysis of asymmetry supports this notion (Figure 4E). However, we were unable to find literature to support this possibility, so it may seem less likely.

With SR101 staining, we showed that L5 astrocyte density remains relatively stable between P3 – P50, which means astrocyte spacing is constant. Therefore, the longer branching of P3 – P10 astrocytes suggests that they might extend into the domains of their neighbors. During maturation, branches may therefore retract to enable the eventual astrocyte tiling in the mature brain. Astrocyte processes retraction is already known to occur, for example, in the supraoptic nucleus during suckling.[45] However, using a different marker, it has been reported that astrocyte density peaks at eye opening and subsequently decays and stabilizes.[40] Additional work is thus required to put this idea to the test.

Astrocytes Ca^{2+} events mature by decorrelating and shortening

Astrocyte Ca^{2+} activity can occur independently of neuronal activity[14,38,46] as well as in response to neuronal activity.[46] Although neuronal activity blockade does not abolish spontaneous Ca^{2+} activity in astrocytes, neuronal activity may regulate astrocyte Ca^{2+} event synchrony, which may affect developmental circuit plasticity.[14,19,37] We showed how spontaneous Ca^{2+} events developed alongside astrocyte electrophysiology and morphology. After ~P15, these Ca^{2+} transients are relatively short, decorrelated, and compartmentalized. Because event correlation and duration cannot become negative, and similarly event frequency cannot increase forever, we argue that these parameters eventually stabilize. A previous theoretical study suggested that morphological profile determines frequency of spontaneous astrocyte Ca^{2+} signals,[47]

specifically that spontaneous Ca^{2+} events start in thin astrocytic processes because of their high surface area-to-volume ratio, which promotes Ca^{2+}-induced Ca^{2+} release. In agreement, computational modeling has reproduced spontaneous Ca^{2+} signals by Ca^{2+}-induced Ca^{2+} release in fine astrocyte processes.[48] These lend support to what we extrapolate from our findings: that increasing complexity from morphological development is associated with the increase in spontaneous Ca^{2+} signals observed over development.

Astrocyte modifications and neuronal plasticity: A two-way street

Over recent years, several studies have revealed examples of astrocyte modulation of neuronal plasticity.[7,8,21,49] For instance, the excitability of medium spiny neurons in the striatum is decreased by reduced astrocyte Ca^{2+} signaling, leading to increased self-grooming behaviors in mice.[50]

Of interest, neurons also modify astrocytes, highlighting a two-way communication. For instance, synaptic plasticity can remodel astrocyte processes.[51] In development, astrocytes can also be modified by molecular cues from neurons, such as neuron-derived sonic hedgehog.[52] In disease models too reorganization of astrocyte processes and loss of astrocyte domains has been observed, e.g., in epilepsy.[53]

Astrocyte maturation is tightly linked to critical period plasticity in the cortex.[7,54] For example, in the mouse visual cortex, an increase in astrocyte connexin 30 has been associated with the closure of the critical period, by inducing the maturation of inhibitory circuits.[7] Our findings add to our understanding of astrocyte changes in morphology and spontaneous Ca^{2+} activity during this critical period.

Conclusions and future directions

Our present work provides a descriptive foundation of astrocyte maturation in developing mouse visual cortex. Because astrocyte Ca^{2+} signaling is key to neocortical plasticity,[21] our findings outline a framework for the study of astrocyte-mediated control of visual cortex critical period plasticity, e.g., by showing that biophysics and Ca^{2+} signaling of visual cortex astrocytes were relatively mature by ~P15, close to eye opening.

As astrocyte branching grew denser, Ca^{2+} signals decorrelated. This was not surprising, because finer arborization should naturally dissociate Ca^{2+} events as branches compartmentalize. Astrocyte morphology, however, continued to mature after P15 when biophysics and dye-coupling were relatively stabilized. Whether maturation of morphology determines developmental decorrelation of astrocyte Ca^{2+} activity thus remains unclear in our hands. Another consideration would be whether these changes in astrocytes are associated with changes in cortical neuronal development around eye opening.[25]

Our study suggests that — like axonal and dendritic arbors[44] — astrocyte branches may initially extend too far and later be pruned, thereby establishing tiling (Figure 6). In the mammalian central nervous system, it is known that astrocytes and microglia participate in axon pruning.[44] If astrocytes themselves are indeed pruned, this raises the intriguing question: who prunes the pruners?

Limitations of the study

A potential caveat is that we measured astrocyte asymmetry in 2D. A 3D analysis might provide more context to the positioning of astrocytes relative to other local structures. For example, Refaeli et al.[55] showed that astrocytes display orientation preference in hippocampus relative to the CA1 pyramidal area. However, a more refined 3D analysis should not alter our overall finding that arborizations mature by growing denser, more compact, and more symmetric.

Another potential caveat is that we pooled morphological data obtained with 2p microscopy of cells dye-loaded during patch-clamp recording with data obtained by confocal imaging after biocytin histology. However, we previously found these methods offered indistinguishable morphological cell classification performance,[56] which justified pooling these types of data. In agreement, each dataset alone offered similar outcome (not shown).

The finest astrocyte compartments cannot be resolved with confocal or 2p microscopy, but require super-resolution or electron microscopy.[57,58] Confocal and 2p imaging may thus underestimate branch numbers and Ca^{2+} signals. However, we had no problems detecting changes in morphology and Ca^{2+} signals across P3 – P50, suggesting a sufficiently detailed resolution for our purposes.

SR101 labels only a subset of astrocytes, although the developmental profile of SR101-positive cells is comparable to that of other astrocytes.[59] In addition, SR101 has limited specificity and may also label oligodendrocytes, although that requires longer incubation time than we used here.[60] Oligodendrocyte morphology is furthermore quite distinct from that of astrocytes.

Some chemical Ca^{2+} indicators suppress Na^+ and K^+-dependent adenosine triphosphatase activity, which may impair cell health.[61] However, when using Fluo-5F, we monitored astrocyte V_m and observed no adverse effects. Furthermore, we only briefly exposed astrocytes to Fluo-5F, typically <30 min.

Finally, in several cases, causation remains to be established. For example, the relationship between gap-junction coupling and R_{input} was correlational, not causal.

STAR★METHODS

Detailed methods are provided in the online version of this paper and include the following:

- KEY RESOURCES TABLE
- RESOURCE AVAILABILITY
  - Lead contact
  - Materials availability
  - Data and code availability
- EXPERIMENTAL MODEL AND SUBJECT DETAILS
- METHOD DETAILS
  - Acute slice electrophysiology
  - Biocytin staining and confocal imaging
  - Two-photon microscopy
  - Morphological reconstruction and analysis
  - Gap-junction coupling quantification
  - Imaging and analysis of spontaneous Ca^{2+} activity
  - Quantifying L5 cortical thickness
  - SR101 cell counts
- QUANTIFICATION AND STATISTICAL ANALYSIS

SUPPLEMENTAL INFORMATION

Supplemental information can be found online at https://doi.org/10.1016/j.isci.2023.106828.

ACKNOWLEDGMENTS

We thank Alanna J. Watt, Hovy Wong, Christina Chou, Sabine Rannio, Amanda McFarlan, Shawniya Alageswaran, Stuart Trenholm, Keith Murai, Aparna Suvrathan, Rui P. Costa, Cian O'Donnell, and members of the Sjöström lab for help and useful discussions. The schematic in Figure 1A was created with BioRender.com.

This work was supported by CFI LOF 28331 (PJS), CIHR PG 156223, FRSQ CB 254033 (PJS), NSERC DG 2017-04730 (PJS), and NSERC DAS 2017-507818 (PJS). A.W. was in receipt of a Healthy Brains Healthy Lives PhD Fellowship, Quebec Bio-Imaging Network PhD Scholarship, and Integrated Program in Neuroscience Studentship. The funders had no role in study design, data collection and interpretation, or the decision to submit the work for publication.

AUTHOR CONTRIBUTIONS

Conceptualization, A.W. and P.J.S.; Methodology, A.W., C.G., and P.J.S.; Software, P.J.S.; Validation, A.W. and P.J.S.; Formal Analysis, A.W. and P.J.S.; Investigation, A.W. and C.G.; Resources, P.J.S.; Data Curation, A.W., C.G., and P.J.S.; Writing – Original Draft, A.W. and P.J.S.; Writing – Reviewing and Editing, A.W. and P.J.S.; Visualization, A.W. and P.J.S.; Supervision, A.W. and P.J.S.; Project Administration, A.W. and P.J.S.; Funding Acquisition, A.W. and P.J.S.

DECLARATION OF INTERESTS

The authors declare no competing interests.

INCLUSION AND DIVERSITY

One or more of the authors of this paper self-identifies as an underrepresented ethnic minority in their field of research or within their geographical location. One or more of the authors of this paper self-identifies as a gender minority in their field of research. One or more of the authors on this paper self-identifies as a member of the LGBTQIA+ community. While citing references scientifically relevant for this work, we also actively worked to promote gender balance in our reference list. We support inclusive, diverse, and equitable conduct of research.

Received: September 30, 2022
Revised: March 8, 2023
Accepted: May 3, 2023
Published: May 6, 2023

REFERENCES

1. Verkhratsky, A., and Nedergaard, M. (2018). Physiology of astroglia. Physiol. Rev. *98*, 239–389. https://doi.org/10.1152/physrev.00042.2016.

2. Cornell-Bell, A.H., Finkbeiner, S.M., Cooper, M.S., and Smith, S.J. (1990). Glutamate induces calcium waves in cultured astrocytes: long-range glial signaling. Science *247*, 470–473. https://doi.org/10.1126/science.1967852.

3. Charles, A.C., Merrill, J.E., Dirksen, E.R., and Sanderson, M.J. (1991). Intercellular signaling in glial cells: calcium waves and oscillations in response to mechanical stimulation and glutamate. Neuron *6*, 983–992. https://doi.org/10.1016/0896-6273(91)90238-u.

4. Nedergaard, M. (1994). Direct signaling from astrocytes to neurons in cultures of mammalian brain cells. Science *263*, 1768–1771. https://doi.org/10.1126/science.8134839.

5. Parpura, V., Basarsky, T.A., Liu, F., Jeftinija, K., Jeftinija, S., and Haydon, P.G. (1994). Glutamate-mediated astrocyte-neuron signalling. Nature *369*, 744–747. https://doi.org/10.1038/369744a0.

6. Giaume, C., Koulakoff, A., Roux, L., Holcman, D., and Rouach, N. (2010). Astroglial networks: a step further in neuroglial and gliovascular interactions. Nat. Rev. Neurosci. *11*, 87–99. https://doi.org/10.1038/nrn2757.

7. Ribot, J., Breton, R., Calvo, C.F., Moulard, J., Ezan, P., Zapata, J., Samama, K., Moreau, M., Bemelmans, A.P., Sabatet, V., et al. (2021). Astrocytes close the mouse critical period for visual plasticity. Science *373*, 77–81. https://doi.org/10.1126/science.abf5273.

8. Allen, N.J., and Eroglu, C. (2017). Cell biology of astrocyte-synapse interactions. Neuron *96*, 697–708. https://doi.org/10.1016/j.neuron.2017.09.056.

9. Weiss, S., Melom, J.E., Ormerod, K.G., Zhang, Y.V., and Littleton, J.T. (2019). Glial Ca^{2+} signaling links endocytosis to K^{+} buffering around neuronal somas to regulate excitability. eLife *8*, e44186. https://doi.org/10.7554/eLife.44186.

10. Kol, A., Adamsky, A., Groysman, M., Kreisel, T., London, M., and Goshen, I. (2020). Astrocytes contribute to remote memory formation by modulating hippocampal-cortical communication during learning. Nat. Neurosci. *23*, 1229–1239. https://doi.org/10.1038/s41593-020-0679-6.

11. Adamsky, A., Kol, A., Kreisel, T., Doron, A., Ozeri-Engelhard, N., Melcer, T., Refaeli, R., Horn, H., Regev, L., Groysman, M., et al. (2018). Astrocytic activation generates de novo neuronal potentiation and memory enhancement. Cell *174*, 59–71.e14. https://doi.org/10.1016/j.cell.2018.05.002.

12. Bushong, E.A., Martone, M.E., Jones, Y.Z., and Ellisman, M.H. (2002). Protoplasmic astrocytes in CA1 stratum radiatum occupy separate anatomical domains. J. Neurosci. *22*, 183–192.

13. Pannasch, U., and Rouach, N. (2013). Emerging role for astroglial networks in information processing: from synapse to behavior. Trends Neurosci. *36*, 405–417. https://doi.org/10.1016/j.tins.2013.04.004.

14. Aguado, F., Espinosa-Parrilla, J.F., Carmona, M.A., and Soriano, E. (2002). Neuronal activity regulates correlated network properties of spontaneous calcium transients in astrocytes in situ. J. Neurosci. *22*, 9430–9444.

15. Perea, G., and Araque, A. (2005). Glial calcium signaling and neuron-glia communication. Cell Calcium *38*, 375–382. https://doi.org/10.1016/j.ceca.2005.06.015.

16. Di Castro, M.A., Chuquet, J., Liaudet, N., Bhaukaurally, K., Santello, M., Bouvier, D., Tiret, P., and Volterra, A. (2011). Local Ca2+ detection and modulation of synaptic release by astrocytes. Nat. Neurosci. *14*, 1276–1284. https://doi.org/10.1038/nn.2929.

17. Grosche, J., Matyash, V., Möller, T., Verkhratsky, A., Reichenbach, A., and Kettenmann, H. (1999). Microdomains for neuron-glia interaction: parallel fiber signaling to Bergmann glial cells. Nat. Neurosci. *2*, 139–143. https://doi.org/10.1038/5692.

18. Perea, G., and Araque, A. (2005). Properties of synaptically evoked astrocyte calcium signal reveal synaptic information processing by astrocytes. J. Neurosci. *25*, 2192–2203. https://doi.org/10.1523/JNEUROSCI.3965-04.2005.

19. Fiacco, T.A., and McCarthy, K.D. (2004). Intracellular astrocyte calcium waves in situ increase the frequency of spontaneous AMPA receptor currents in CA1 pyramidal neurons. J. Neurosci. *24*, 722–732. https://doi.org/10.1523/JNEUROSCI.2859-03.2004.

20. Volterra, A., and Meldolesi, J. (2005). Astrocytes, from brain glue to communication elements: the revolution continues. Nat. Rev. Neurosci. *6*, 626–640. https://doi.org/10.1038/nrn1722.

21. Min, R., and Nevian, T. (2012). Astrocyte signaling controls spike timing-dependent depression at neocortical synapses. Nat. Neurosci. *15*, 746–753. https://doi.org/10.1038/nn.3075.

22. Espinosa, J.S., and Stryker, M.P. (2012). Development and plasticity of the primary visual cortex. Neuron *75*, 230–249. https://doi.org/10.1016/j.neuron.2012.06.009.

23. Sawtell, N.B., Frenkel, M.Y., Philpot, B.D., Nakazawa, K., Tonegawa, S., and Bear, M.F. (2003). NMDA receptor-dependent ocular dominance plasticity in adult visual cortex. Neuron *38*, 977–985.

24. Hoy, J.L., and Niell, C.M. (2015). Layer-specific refinement of visual cortex function after eye opening in the awake mouse. J. Neurosci. *35*, 3370–3383. https://doi.org/10.1523/JNEUROSCI.3174-14.2015.

25. Ciganok-Hückels, N., Jehasse, K., Kricsfalussy-Hrabár, L., Ritter, M., Rüland, T., and Kampa, B.M. (2022). Postnatal development of electrophysiological and morphological properties in layer 2/3 and layer 5 pyramidal neurons in the mouse primary visual cortex. Cerebr. Cortex. https://doi.org/10.1093/cercor/bhac467.

26. Bushong, E.A., Martone, M.E., and Ellisman, M.H. (2004). Maturation of astrocyte morphology and the establishment of astrocyte domains during postnatal hippocampal development. Int. J. Dev. Neurosci. *22*, 73–86. https://doi.org/10.1016/j.ijdevneu.2003.12.008.

27. Isokawa, M., and McKhann, G.M., 2nd (2005). Electrophysiological and morphological characterization of dentate astrocytes in the hippocampus. J. Neurobiol. *65*, 125–134. https://doi.org/10.1002/neu.20186.

28. Nimmerjahn, A., and Helmchen, F. (2012). In vivo labeling of cortical astrocytes with sulforhodamine 101 (SR101). Cold Spring Harb. Protoc. *2012*, 326–334. https://doi.org/10.1101/pdb.prot068155.

29. Nimmerjahn, A., Kirchhoff, F., Kerr, J.N.D., and Helmchen, F. (2004). Sulforhodamine 101 as a specific marker of astroglia in the neocortex in vivo. Nat. Methods *1*, 31–37. https://doi.org/10.1038/nmeth706.

30. Adermark, L., and Lovinger, D.M. (2008). Electrophysiological properties and gap junction coupling of striatal astrocytes. Neurochem. Int. *52*, 1365–1372. https://doi.org/10.1016/j.neuint.2008.02.006.

31. Chai, H., Diaz-Castro, B., Shigetomi, E., Monte, E., Octeau, J.C., Yu, X., Cohn, W., Rajendran, P.S., Vondriska, T.M., Whitelegge, J.P., et al. (2017). Neural circuit-specialized astrocytes: transcriptomic, proteomic, morphological, and functional evidence. Neuron *95*, 531–549.e9. https://doi.org/10.1016/j.neuron.2017.06.029.

32. Schools, G.P., Zhou, M., and Kimelberg, H.K. (2006). Development of gap junctions in hippocampal astrocytes: evidence that whole cell electrophysiological phenotype is an intrinsic property of the individual cell. J. Neurophysiol. *96*, 1383–1392. https://doi.org/10.1152/jn.00449.2006.

33. Stephan, J., Eitelmann, S., and Zhou, M. (2021). Approaches to study gap junctional coupling. Front. Cell. Neurosci. *15*, 640406. https://doi.org/10.3389/fncel.2021.640406.

34. Breithausen, B., Kautzmann, S., Boehlen, A., Steinhäuser, C., and Henneberger, C. (2020). Limited contribution of astroglial gap junction coupling to buffering of extracellular K^+ in CA1 stratum radiatum. Glia *68*, 918–931. https://doi.org/10.1002/glia.23751.

35. Rozental, R., Srinivas, M., and Spray, D.C. (2001). How to close a gap junction channel. In Connexin Methods and Protocols, R. Bruzzone and C. Giaume, eds. (Humana Press), pp. 447–476. https://doi.org/10.1385/1-59259-043-8:447.

36. Sholl, D.A. (1953). Dendritic organization in the neurons of the visual and motor cortices of the cat. J. Anat. *87*, 387–406.

37. Parri, H.R., Gould, T.M., and Crunelli, V. (2001). Spontaneous astrocytic Ca^{2+} oscillations in situ drive NMDAR-mediated neuronal excitation. Nat. Neurosci. *4*, 803–812. https://doi.org/10.1038/90507.

38. Nett, W.J., Oloff, S.H., and McCarthy, K.D. (2002). Hippocampal astrocytes in situ exhibit calcium oscillations that occur independent of neuronal activity. J. Neurophysiol. *87*, 528–537. https://doi.org/10.1152/jn.00268.2001.

39. Wang, Y., DelRosso, N.V., Vaidyanathan, T.V., Cahill, M.K., Reitman, M.E., Pittolo, S., Mi, X., Yu, G., and Poskanzer, K.E. (2019). Accurate quantification of astrocyte and neurotransmitter fluorescence dynamics for single-cell and population-level physiology. Nat. Neurosci. *22*, 1936–1944. https://doi.org/10.1038/s41593-019-0492-2.

40. Wang, L.L., Xu, D., Luo, Y., Li, X., Gu, Y., and Wang, L. (2022). Homeostatic regulation of astrocytes by visual experience in the developing primary visual cortex. Cereb. Cortex *32*, 970–986. https://doi.org/10.1093/cercor/bhab259.

41. McKhann, G.M., D'Ambrosio, R., and Janigro, D. (1997). Heterogeneity of astrocyte resting membrane potentials and intercellular coupling revealed by whole-cell and gramicidin-perforated patch recordings from cultured neocortical and hippocampal slice astrocytes. J. Neurosci. *17*, 6850–6863.

42. Anders, S., Minge, D., Griemsmann, S., Herde, M.K., Steinhäuser, C., and Henneberger, C. (2014). Spatial properties of astrocyte gap junction coupling in the rat hippocampus. Philos. Trans. R. Soc. Lond. B Biol. Sci. *369*, 20130600. https://doi.org/10.1098/rstb.2013.0600.

43. Griemsmann, S., Höft, S.P., Bedner, P., Zhang, J., von Staden, E., Beinhauer, A., Degen, J., Dublin, P., Cope, D.W., Richter, N., et al. (2015). Characterization of panglial gap junction networks in the thalamus, neocortex, and Hippocampus reveals a unique population of glial cells. Cereb. Cortex *25*, 3420–3433. https://doi.org/10.1093/cercor/bhu157.

44. Riccomagno, M.M., and Kolodkin, A.L. (2015). Sculpting neural circuits by axon and dendrite pruning. Annu. Rev. Cell Dev. Biol. *31*, 779–805. https://doi.org/10.1146/annurev-cellbio-100913-013038.

45. Wang, Y.F., and Hatton, G.I. (2009). Astrocytic plasticity and patterned oxytocin neuronal activity: dynamic interactions. J. Neurosci. *29*, 1743–1754. https://doi.org/10.1523/JNEUROSCI.4669-08.2009.

46. Honsek, S.D., Walz, C., Kafitz, K.W., and Rose, C.R. (2012). Astrocyte calcium signals at Schaffer collateral to CA1 pyramidal cell synapses correlate with the number of activated synapses but not with synaptic strength. Hippocampus *22*, 29–42. https://doi.org/10.1002/hipo.20843.

47. Wu, Y.W., Gordleeva, S., Tang, X., Shih, P.Y., Dembitskaya, Y., and Semyanov, A. (2019). Morphological profile determines the frequency of spontaneous calcium events in astrocytic processes. Glia *67*, 246–262. https://doi.org/10.1002/glia.23537.

48. Denizot, A., Arizono, M., Nägerl, U.V., Soula, H., and Berry, H. (2019). Simulation of calcium signaling in fine astrocytic processes: effect of spatial properties on spontaneous activity. PLoS Comput. Biol. *15*, e1006795. https://doi.org/10.1371/journal.pcbi.1006795.

49. Falcón-Moya, R., Pérez-Rodríguez, M., Prius-Mengual, J., Andrade-Talavera, Y., Arroyo-García, L.E., Pérez-Artés, R., Mateos-Aparicio, P., Guerra-Gomes, S., Oliveira, J.F., Flores, G., and Rodríguez-Moreno, A. (2020). Astrocyte-mediated switch in spike timing-dependent plasticity during hippocampal development. Nat. Commun. *11*, 4388. https://doi.org/10.1038/s41467-020-18024-4.

50. Yu, X., Taylor, A.M.W., Nagai, J., Golshani, P., Evans, C.J., Coppola, G., and Khakh, B.S. (2018). Reducing astrocyte calcium signaling in vivo alters striatal microcircuits and causes repetitive behavior. Neuron *99*, 1170–1187.e9. https://doi.org/10.1016/j.neuron.2018.08.015.

51. Perez-Alvarez, A., Navarrete, M., Covelo, A., Martin, E.D., and Araque, A. (2014). Structural and functional plasticity of astrocyte processes and dendritic spine interactions. J. Neurosci. *34*, 12738–12744. https://doi.org/10.1523/JNEUROSCI.2401-14.2014.

52. Farmer, W.T., Abrahamsson, T., Chierzi, S., Lui, C., Zaelzer, C., Jones, E.V., Bally, B.P., Chen, G.G., Théroux, J.F., Peng, J., et al. (2016). Neurons diversify astrocytes in the adult brain through sonic hedgehog signaling. Science *351*, 849–854. https://doi.org/10.1126/science.aab3103.

53. Oberheim, N.A., Tian, G.F., Han, X., Peng, W., Takano, T., Ransom, B., and Nedergaard, M. (2008). Loss of astrocytic domain organization in the epileptic brain. J. Neurosci. *28*, 3264–3276. https://doi.org/10.1523/JNEUROSCI.4980-07.2008.

54. Ackerman, S.D., Perez-Catalan, N.A., Freeman, M.R., and Doe, C.Q. (2021). Astrocytes close a motor circuit critical period. Nature *592*, 414–420. https://doi.org/10.1038/s41586-021-03441-2.

55. Refaeli, R., Doron, A., Benmelech-Chovav, A., Groysman, M., Kreisel, T., Loewenstein, Y., and Goshen, I. (2021). Features of hippocampal astrocytic domains and their spatial relation to excitatory and inhibitory neurons. Glia *69*, 2378–2390. https://doi.org/10.1002/glia.24044.

56. Blackman, A.V., Grabuschnig, S., Legenstein, R., and Sjöström, P.J. (2014). A comparison of manual neuronal reconstruction from biocytin histology or 2-photon imaging: morphometry and computer modeling. Front. Neuroanat. *8*, 65. https://doi.org/10.3389/fnana.2014.00065.

57. Arizono, M., Idziak, A., Quici, F., and Nägerl, U.V. (2023). Getting sharper: the brain under the spotlight of super-resolution microscopy. Trends Cell Biol. *33*, 148–161. https://doi.org/10.1016/j.tcb.2022.06.011.

58. Salmon, C.K., Syed, T.A., Kacerovsky, J.B., Alivodej, N., Schober, A.L., Sloan, T.F.W., Pratte, M.T., Rosen, M.P., Green, M., Chirgwin-Dasgupta, A., et al. (2023). Organizing principles of astrocytic nanoarchitecture in the mouse cerebral cortex. Curr. Biol. *33*, 957–972.e5. https://doi.org/10.1016/j.cub.2023.01.043.

59. Kafitz, K.W., Meier, S.D., Stephan, J., and Rose, C.R. (2008). Developmental profile and properties of sulforhodamine 101–Labeled glial cells in acute brain slices of rat hippocampus. J. Neurosci. Methods *169*, 84–92. https://doi.org/10.1016/j.jneumeth.2007.11.022.

60. Hill, R.A., and Grutzendler, J. (2014). In vivo imaging of oligodendrocytes with sulforhodamine 101. Nat. Methods *11*, 1081–1082. https://doi.org/10.1038/nmeth.3140.

61. Smith, N.A., Kress, B.T., Lu, Y., Chandler-Militello, D., Benraiss, A., and Nedergaard, M. (2018). Fluorescent Ca2+ indicators directly inhibit the Na,K-ATPase and disrupt cellular functions. Sci. Signal. *11*, eaal2039. https://doi.org/10.1126/scisignal.aal2039.

62. Myatt, D.R., Hadlington, T., Ascoli, G.A., and Nasuto, S.J. (2012). Neuromantic - from semi-manual to semi-automatic reconstruction of neuron morphology. Front. Neuroinform. *6*, 4. https://doi.org/10.3389/fninf.2012.00004.

63. Zhou, L., Nho, K., Haddad, M.G., Cherepacha, N., Tubeleviciute-Aydin, A., Tsai, A.P., Saykin, A.J., Jesper Sjöström, P., and LeBlanc, A.C. (2021). Rare CASP6N73T variant associated with hippocampal volume exhibits decreased proteolytic activity, synaptic transmission defect, and neurodegeneration. Sci. Rep. *11*, 12695. https://doi.org/10.1038/s41598-021-91367-0.

64. Schindelin, J., Arganda-Carreras, I., Frise, E., Kaynig, V., Longair, M., Pietzsch, T., Preibisch, S., Rueden, C., Saalfeld, S., Schmid, B., et al. (2012). Fiji: an open-source platform for biological-image analysis. Nat. Methods *9*, 676–682. https://doi.org/10.1038/nmeth.2019.

65. Abrahamsson, T., Chou, C.Y.C., Li, S.Y., Mancino, A., Costa, R.P., Brock, J.A., Nuro, E., Buchanan, K.A., Elgar, D., Blackman, A.V., et al. (2017). Differential regulation of evoked and spontaneous release by presynaptic NMDA receptors. Neuron *96*, 839–855.e5. https://doi.org/10.1016/j.neuron.2017.09.030.

66. Reynolds, S., Abrahamsson, T., Schuck, R., Sjöström, P.J., Schultz, S.R., and Dragotti, P.L. (2017). ABLE: an activity-based level set segmentation algorithm for two-photon calcium imaging data. eNeuro *4*. https://doi.org/10.1523/ENEURO.0012-17.2017.

67. Agarwal, A., Wu, P.H., Hughes, E.G., Fukaya, M., Tischfield, M.A., Langseth, A.J., Wirtz, D., and Bergles, D.E. (2017). Transient opening of the mitochondrial permeability transition pore induces microdomain calcium transients in astrocyte processes. Neuron *93*, 587–605.e7. https://doi.org/10.1016/j.neuron.2016.12.034.

STAR★METHODS

KEY RESOURCES TABLE

REAGENT or RESOURCE	SOURCE	IDENTIFIER
Chemicals, peptides, and recombinant proteins		
Streptavidin, Alexa Fluor™ 647 Conjugate	Thermo Fisher Scientific	S32357
Alexa Fluor™ 594 hydrazide	Life Technologies	A10438
Alexa Fluor™ 488 hydrazide	Life Technologies	A10436
Carbenoxolone disodium salt	Sigma-Aldrich	C4790
Fluo-5F, pentapotassium salt	Fisher Scientific	F14221
Normal Donkey Serum	Jackson ImmunoResearch	017-000-121
Sulforhodamine 101	Millipore Sigma	S7635
Experimental models: Organisms/strains		
C57BL/6J	The Jackson Laboratory	Strain #000664; RRID:IMSR_JAX:000664
Software and algorithms		
Neuromantic	https://www.reading.ac.uk/neuromantic/body_index.php	V1.7.5; Myatt, et al., 2012[62]
Igor Pro	WaveMetrics	Igor Pro 8 and 9
MultiPatch	https://github.com/pj-sjostrom/MultiPatch.git	https://doi.org/10.5281/zenodo.7854025
qMorph	https://github.com/pj-sjostrom/qMorph	Zhou et al., 2021[63]; https://doi.org/10.5281/zenodo.7853963
Linescan analysis	https://github.com/pj-sjostrom/LineScanAnalysis	This paper; https://doi.org/10.5281/zenodo.7853953
FIJI	https://imagej.net/software/fiji/	Schindelin at al, 2012[64]
AQuA	https://github.com/yu-lab-vt/AQuA	Wang, et al. 2019[39]
ScanImage	https://www.mbfbioscience.com/products/scanimage	2019 - 2022

RESOURCE AVAILABILITY

Lead contact

Further information and requests for resources and reagents should be directed to and will be fulfilled by the lead contact, Jesper Sjöström (jesper.sjostrom@mcgill.ca).

Materials availability

This study did not generate new unique reagents.

Data and code availability

- All data reported in this paper will be shared by the lead contact upon request.
- All original code has been deposited on Zenodo and is publicly available as of the date of publication. DOIs are listed in the key resources table.
- Any additional information required to reanalyze the data reported in this paper is available from the lead contact upon request.

EXPERIMENTAL MODEL AND SUBJECT DETAILS

The animal study was reviewed and approved by the Montreal General Hospital Facility Animal Care Committee (The MGH FACC) and adhered to the guidelines of the Canadian Council on Animal Care (CCAC). Female and male C57BL/6J mice (000664; The Jackson Laboratory) aged P3 - P50 were subjected to a 12h

light and 12h dark cycle with food and water provided *ad libitum*. Mice were anesthetized using isoflurane and sacrificed by decapitation after the loss of the hind-limb withdrawal reflex was confirmed.

METHOD DETAILS

Acute slice electrophysiology

After decapitation, the brain was removed and placed in ice-cold (~4°C) artificial cerebrospinal fluid (ACSF), containing in mM: 125 NaCl, 2.5 KCl, 1 $MgCl_2$, 1.25 NaH_2PO_4, 2 $CaCl_2$, 26 $NaHCO_3$ and 25 glucose, bubbled with 95% O_2/5% CO_2 (carbogen). Osmolality of the ACSF was adjusted to ~338 ± 3 mOsm with glucose. Oblique coronal 300-μm-thick acute brain slices were prepared using a Campden Instruments 5000 mz-2 vibratome (Lafayette Instrument, Lafayette, IN, USA). Brain slices were kept at ~33°C in oxygenated ACSF for ~30 min and then allowed to cool at room temperature for at least one hour after slicing before patching. For mice ~P25 and older, we used 2 mM $MgCl_2$ and 1 mM $CaCl_2$ in the ACSF during slicing and recovery, and standard ACSF as described above for patching.

Glass pipettes (3 – 7 MΩ) were used for whole-cell recordings and were filled with internal solution (in mM: KCl, 5; K-Gluconate, 115; HEPES, 10; Mg-ATP, 4; Na-GTP, 0.3; Na-Phosphocreatine, 10; Biocytin, 0.1% w/v; adjusted with KOH to pH 7.2 and with sucrose to ~310 ± 3 mOsm, and supplemented with Alexa Fluor 594 or 488, 20 - 80 μM). We carried out electrophysiology experiments with ACSF heated to 32-34°C with a resistive inline heater (Scientifica Ltd, UK), with temperature continuously recorded and verified offline.

BVC-700A (Dagan Corporation, Minneapolis, MN) and Model 2400 (A-M Systems, Carlsborg, WA) amplifiers were used to obtain whole-cell recordings. Amplified signals were filtered at 5 kHz and sampled at 40 kHz using PCI-6229 boards (NI, Austin, TX, USA) with MultiPatch custom software (https://doi.org/10.5281/zenodo.7854025) running in Igor Pro 8 or 9 (WaveMetrics Inc., Lake Oswego, OR, USA).

Astrocytes were selectively stained by incubating slices in 1 or 5 μM sulforhodamine 101 (SR101) solution[28,29] made up in standard ACSF for 5 minutes at room temperature while bubbling with carbogen. SR101-positive astrocytes were then visualized with two-photon (2p) microscopy at 820 nm or 930 nm and targeted for whole-cell patching. After patching in current clamp, cell identity was confirmed by checking for a low resting V_m (~-70 mV), low R_{input} (<100 MΩ), and by injecting currents from -0.3 to 0.7 nA at 0.2 nA increments to verify that they did not exhibit action potentials. Resting V_m and R_{input} of each cell were measured from a 10-ms-long window and a 250-ms-long 25-pA hyperpolarizing test pulse, respectively, at the beginning of each current step and taken as an average from six waves. Bushy morphology was confirmed post-hoc with 2p imaging. Recordings were not corrected for liquid junction potential (~10 mV) or for series resistance. Throughout this study, recordings were discarded or truncated if V_m changed by >20 mV or if R_{input} changed by >40 MΩ.

To generate IV curves, astrocytes were voltage clamped at -80 mV and voltage steps from +60 mV to -160 mV at 20 mV decrements were applied for 500 ms. To quantify the passivity of the astrocyte, current readings were taken at 10 ms after the beginning of the voltage step ("Early") and 10 ms before the end of the voltage step ("Late") and the difference between the slope of the last 5 Late and last 5 Early readings were taken as the change in conductance (ΔConductance) across the voltage step over age.

Biocytin staining and confocal imaging

Astrocytes were recorded in whole-cell configuration for at least 15 minutes to allow for biocytin diffusion. To ensure re-sealing of cell membrane during pipette removal, cells were held at a depolarizing potential (-40 to -30 mV) while the pipette was slowly removed along the diagonal axis. The acute slice was fixed in 4% paraformaldehyde (PFA) overnight at 4°C and then transferred to 0.1 M phosphate buffered saline (PBS) for up to one week before staining.

Acute slices were washed four times in 10 mM Tris-buffered saline (TBS) solution with 0.3% Triton-X for 10 minutes each. Slices were blocked with 10 mM TBS with 0.3% Triton-X and 10% normal donkey serum (NDS; 017-000-121 Jackson ImmunoResearch, West Grove, PA, USA) for 1 hour. Alexa Fluor 647-conjugated streptavidin (S32357 ThermoFisher Scientific, Waltham, MA, USA) at 1:200 dilution in 0.01 M TBS with 0.3% Triton-X and 1% Normal Donkey Serum was used to bind to biocytin overnight at 4°C. Slices were then washed four times in 10 mM TBS solution for 10 minutes each. The slices were

mounted on glass slides with ProLong Gold Antifade Mountant (ThermoFisher Scientific, Waltham, MA, USA) and clear nail polish was applied around the coverslip perimeter.

Image stacks were acquired with 633 nm laser-line excitation using a Zeiss LSM 780 confocal microscope, at 20× or 40× magnification and 1024×1024-pixel resolution centered around the patched soma, controlled by the ZEN2010 software (ZEISS International, Jena, Germany).

Two-photon microscopy

2p laser-scanning microscopy was performed with a custom-built imaging workstation, as previously described.[65] 2p excitation was achieved using a titanium-sapphire laser tuned to 820 nm for Alexa-594, and 930 nm for Alexa-488. Laser power output was monitored using a power meter and was controlled by adjusting a half-lambda plate passing the laser beam to a polarizing beam-splitting cube (Thorlabs GL10-B and AHWP05M-980). Laser gating was achieved with a mechanical shutter (Thorlabs SH05/SC10) triggered by software and scanning was achieved with 6215H 3-mm galvanometric mirrors (Cambridge Technology, Bedford, MA). Bialkali photomultipliers (Scientifica 2PIMS-2000-20-20) detected fluorescence via an Olympus LUMPlanFL N 40×/0.80 objective. Fluorescence was separated with Semrock FF665 and laser light blocked with Semrock FF01-680. Red and green fluorescence were separated with Chroma t565lxpr combined with Chroma ET630/75M and Chroma ET525/50M. Laser-scanning Dodt contrast was achieved with custom optics, by collecting laser light that passed through the acute slice with a spatial filter and a diffuser placed in a 1× telescope with an amplified diode (Thorlabs PDA100A-EC). Signals from photomultipliers and diode were acquired with a PCI-6110 digitization board (NI, Austin, TX, USA) using ScanImage 2019-2022 running in MATLAB (The MathWorks, Natick, MA, USA). Ca^{2+} imaging data was analyzed with the custom script LineScanAnalysis (https://doi.org/10.5281/zenodo.7853953) running in Igor Pro 9.

Morphological reconstruction and analysis

After each whole-cell recording, cell morphologies were acquired with the 40× objective as stacks of 512×512-pixel slices with 1 μm between each slice. Each slice is an average of 2 – 3 frames. These 3D stacks were *Z*-projected by maximum intensity, pseudo-colored, and assembled using Fiji.[64]

Prior to reconstruction, brightness and contrast were adjusted in Fiji to ensure that branches in 3D stacks were optimally visible. Cells were then reconstructed by manual tracing using Neuromantic.[62] Reconstructed morphologies were analyzed with the qMorph in-house software[63] (https://doi.org/10.5281/zenodo.7853963), running in Igor Pro 9.

Gap-junction coupling quantification

To quantify gap-junction coupling in astrocytes, individual cells were patched and filled with biocytin for 15 minutes. For a subset of experiments, carbenoxolone was either added to the internal solution (20 μM) or washed in (50 μM) 10 minutes prior to patching.[34] Biocytin-filled cells were fixed in PFA and stained, as described above. *Z*-stack images were acquired 25 μm above and 25 μm below the center of the patched cell soma with confocal imaging at 20× magnification as described above. Using the Cell Counter Plugin in Fiji, the number of fluorescent neighboring astrocyte soma was counted as a measure of amount of coupling.

Imaging and analysis of spontaneous Ca^{2+} activity

Astrocytes were patched with glass pipettes loaded with Fluo-5F (200 μM) for 15 - 20 minutes. Using 2p excitation at 930 nm, the cell was imaged at a single focal plane for 180 s, using 256×256 or 512×512-pixel frames acquired at 2.1 – 4.2 Hz frame rate. Ca^{2+} signals were measured as dG/R, i.e., a change in green Fluo-5F fluorescence normalized to SR101 fluorescence acquired in the red channel.

At least 10 regions of interest (ROIs) of similar size were manually selected. We avoided automated ROI selection methods[39,66,67] because we were concerned that ROI selection methods that rely on signal evolution might affect Ca^{2+} signal decorrelation measurements, since automated ROI selection relies on the time evolution of pixel signal correlations. Baseline was set at the 10 – 40 frames with the weakest Ca^{2+} signal. To eliminate high-frequency noise, signal was low-pass filtered at 0.2 Hz. Mean *Z*-scores of Pearson's r for the correlation of all ROIs were used to measure correlation of astrocyte Ca^{2+} activity.

Ca^{2+} events were detected by and counted with a simple thresholding algorithm, with the threshold detection level set at 1 – 1.5 sigma above background noise. Ca^{2+} event duration was similarly defined by the time during which the signal crossed this threshold. Frequency of Ca^{2+} activity was calculated by taking the total number of events detected divided by the total number ROIs selected for the cell and obtaining the number of events per ROI for each cell.

Automated event detection was carried out with AQuA[39] implemented in MATLAB (The MathWorks, Natick, MA, USA). We restricted the detection area to the region of the single astrocyte. Noise standard deviation (sigma) was estimated by AQuA. The intensity threshold scaling factor (thrARScl) for pixel activity detection was set to 8 times sigma. Spatial gaussian filtering (smoXY) was set to 0.5 sigma, and the minimum pixel size (minSize) for detection was set between 7 and 22 pixels, depending on the resolution of the movie. Temporal cut threshold (thrTWScl), which distinguishes separate events in the same space was set to 8 times sigma. *Z*-score threshold (zThr) was set to 5 to conservatively distinguish actual events from noise. Events lower than 40% of peak ΔF (minShow1 = 0.4) and <0.2 s duration (seedRemoveNeib = 2) were discarded.

Quantifying L5 cortical thickness

The thickness of cortical L5 was measured from confocal and 2p images using the brightfield and Dodt contrast channels, respectively. The upper and lower L5 boundaries were determined by visual inspection, with L5 pyramidal cells identified by their large soma and prominent apical dendrites. For each brain slice, the L5 thickness was measured in either Fiji or Affinity Designer (Serif, Nottingham, UK). Using Igor Pro 9, a sigmoid was numerically fitted to data.

SR101 cell counts

Stacks of 256×256 or 512×512-pixel images were obtained with ScanImage at 2× zoom from acute slices that were incubated in 1 μM SR101 for 5 minutes. Brightness and contrast were automatically set in Fiji, using histogram normalization. Cells were counted in one acute slice every ~3 - 10 μm in each stack. Dim cells or cells with incomplete soma were not counted. Cell counts for each stack were done at 3 different starting points and the average was taken to obtain cell density.

QUANTIFICATION AND STATISTICAL ANALYSIS

Unless otherwise noted, results are reported as the mean ± standard error of the mean (SEM). Significance levels are denoted using asterisks (*$p < 0.05$, **$p < 0.01$, ***$p < 0.001$) and can be found in the figures. Sample sizes can be found in the figure legends. Statistical tests were performed in Igor Pro 9. Pairwise comparisons were carried out using the two-tailed Student's t-test for equal means. If the equality of variances F-test gave $p < 0.05$, we employed the unequal variances t-test. In Figures 1A and 1B, cells with either outlying V_m or outlying R_{input} as identified using Tukey's fences were excluded from the analysis (34 cells excluded out of 256). The Wilcoxon-Mann-Whitney rank test was used to test carbenoxolone cell counts in Figure 3F. In Figure 4E, we applied the Welch ANOVA. A t-test on Pearson's r or the Wilcoxon-Mann-Whitney test on Spearman's rho was used to determine significance of correlations. Sigmoids of the form $base + \frac{max}{1+e^{(x_{half}-x)/rate}}$ were numerically fitted in Igor Pro.